Microstructure development of quenching and partitioning-processed martensitic stainless steels with different manganese content

Li, Gaojie; Kwakernaak, Cees; Smith, Ali; Muratori, Marta; Gonzalez-Garcia, Yaiza; Santofimia, Maria J.

Important note
To cite this publication, please use the final published version (if applicable).
Please check the document version above.

Microstructure development of quenching and partitioning-processed martensitic stainless steels with different manganese content

Gaojie Li[1], Cees Kwakernaak[1], Ali Smith[2], Marta Muratori[3], Yaiza Gonzalez-Garcia[1] and Maria J. Santofimia[1]

Abstract
This work presents an investigation of the microstructure development during the application of the quenching and partitioning (Q&P) process to two stainless steels with different Mn content. The results are compared with calculations based on the constrained carbon equilibrium theory, paying special attention to the presence of reactions competing for the carbon available for partitioning and to the effect of alloying element segregation. Results show that chromium carbides must be considered when accounting for the carbon available for austenite stabilisation. Moreover, manganese/chromium segregation bands play an important role in the microstructure development, particularly in martensite formation, with important consequences in the microstructure development during the following processing steps.

Keywords
quenching and partitioning, martensitic stainless steels, segregation, microstructure

Highlights

- The CCE model cannot be directly applied to the studied quenching and partitioning-treated martensitic stainless steels due to carbide precipitation.
- Carbon content in austenite at the partitioning temperature is best estimated from the *Ms* temperature obtained by sub-zero quench in the dilatometer.
- Mn and Cr segregation bands were detected leading to a local *Ms* temperature scatter up to 90°C.
- The alloy with 3.00 wt% Mn displays larger heterogeneity of carbon in the microstructure and larger *Ms* temperature scatter than the alloy with 0.77 wt% Mn.
- Combining the Koistinen–Marburger model and EPMA measurements enabled the local characterisation of martensite formation kinetics.

Introduction

The quenching and partitioning (Q&P) process is a heat treatment originally introduced for creating advanced high-strength steels (AHSSs) with microstructures containing retained austenite (RA) in a martensitic matrix, leading to good combinations of strength and ductility.[1–3]

The Q&P process consists of four steps: (1) the austenitisation step, during which the steel is fully or partially austenitised and the characteristics of the parent austenite like grain size, composition homogeneity and morphology can be controlled via appropriate heat treatment parameters; (2) the quenching step, during which the austenitised microstructure is quenched to a temperature between the martensite start (Ms) temperature and the martensite finish (Mf) temperature, aiming to obtain a controlled combination of austenite and martensite in the microstructure; (3) the partitioning step, in which the material is kept at a constant temperature (same or higher than the quenching temperature) to promote the redistribution of carbon from martensite to austenite[4–6] and (4) the final quenching step, during which the partitioned microstructure is cooled down to room temperature (RT), and fresh martensite may form. The formation of

[1]Department of Materials Science and Engineering, Delft University of Technology, Delft, The Netherlands
[2]Centro Sviluppo Materiali-RINA Consulting, Rome, Italy
[3]Acerinox Europa S.A.U., Acerinox Europa, Los Barrios, Spain

Corresponding author:
Gaojie Li, Department of Materials Science and Engineering, Delft University of Technology, Mekelweg 2, 2628 CD, Delft, The Netherlands.
Email: g.li-6@tudelft.nl

fresh martensite is normally avoided as it damages the ductility of steels.[5–7]

The process of carbon partitioning from martensite into austenite is essential for austenite stabilisation, of which the thermodynamics was initially described by the constrained carbon equilibrium (CCE) model proposed by Speer.[2] The CCE model considers that the process of carbon partitioning takes place under the following three conditions: (1) the process of carbon partitioning continues until the chemical potential of carbon in martensite and austenite equilibrates; (2) the martensite/austenite interface remains immobile during this process and (3) no competitive reactions, such as carbide precipitation and austenite decomposition, take place. The CCE model can be also applied to predict the quenching temperature leading to a maximum in the volume fraction of RA, for which the three aforementioned conditions are coupled with equations describing martensite transformation kinetics.[8] However, studies found that the CCE model is unlikely to be satisfied during actual Q&P processing because carbide precipitation and other competing reactions may take place in steels.[9–11] Competing reactions consume carbon that otherwise should be available for partitioning into the austenite. These observations led to adaptations of the CCE model taking into account competing processes.[12–16]

The application of the CCE model to describe the carbon partitioning process during the application of Q&P heat treatments to stainless steels has been less investigated than in carbon steels. Several authors have found that the CCE model is not directly applicable to stainless steels due to the presence of competing reactions. For example, the carbon content present in RA has been found to deviate with respect to the expected according to the CCE assumptions due to the occurrence of carbide precipitation.[17–20] The occurrence of austenite reversion may also take place, affecting the fraction of phase constituents.[17] Martensite/austenite interface migration, driven by the difference in the chemical potential of the metal atoms (Fe–Cr), was also revealed.[20] In contrast to those previous observations, the nearly ideal CCE condition was realised with the appropriate addition of Si,[21] indicating that the applicability of the CCE model also relates to special elements that could inhibit the competing reactions.

Different alloying elements are considered in the design of Q&P steels, with carbon being the main element, while Mn, Si, Al and Cr are added for their important roles in suppressing the formation of cementite and stabilising RA.[22,23] Among these alloying elements, Mn is added to promote austenitic microstructures by lowering the free energy of austenite, stabilising the phase.[24] However, Mn segregation is frequent in most Mn-alloyed steels.[25–30] For the case of carbon steels processed by the Q&P process, several studies indicate the presence of Mn segregation. In particular, Mn segregation produces banded microstructures during the Q&P process since it affects the local Ms temperature,[26–28] which can cause large hardness gradients and trigger different fracture mechanisms.[29,30] Microstructural bands and inhomogeneity in these cases can be minimised by applying lower quenching temperatures to decrease the difference between the fraction of primary martensite among the bands.[27,31]

Cr is an essential alloying element to provide corrosion resistance in stainless steel. Cr addition inhibits bainite formation, which simplifies microstructure control during the application of the Q&P process in stainless steels with respect to carbon steels.[19] Theoretically, Cr was assumed to replace the role of Si in retarding the formation of carbides[19,21] because Cr reduces carbon diffusivity in austenite by decreasing carbon thermodynamic activity. In earlier studies focused on stainless steels, researchers noted the presence of $M_{23}C_6$-type Cr-carbides in ferritic stainless steels after undergoing the Q&P treatment.[32,33] However, a key question remains unanswered: whether these carbides formed during the initial quenching[27] or during the subsequent partitioning step. In contrast, when examining Q&P-treated martensitic stainless steels in prior research,[17–21,34] investigators consistently detected M_3C and M_7C_3 carbides within the martensitic structure, but there was no evidence of $M_{23}C_6$ carbides in any of the studies conducted. The high content of Cr in stainless steels raised concerns regarding elemental segregation due to its low diffusion in steels,[35,36] although Cr segregation has only been observed in one Cr-containing Q&P-treated medium carbon steel.[31] If that is the case, Cr segregation may have an effect on the microstructure homogeneity and the local presence of Cr-carbides.

Based on the analysis conducted earlier, it is evident that carbide precipitation may not be completely prevented, leading to competition with the "pure partitioning" process, consequently influencing microstructure evolution. This observation raises two intriguing questions that remain unexplored with regard to the suitability of the Q&P process for martensitic stainless steels. The first aspect is determining which are the most relevant processes competing for the carbon available for carbon partitioning in this type of steel and how they affect the applicability of the CCE model. The second aspect is to elucidate the influence of chromium/manganese band segregation, present in stainless steels, on the microstructure development. In order to answer these questions, this work investigates the microstructure development under different Q&P conditions in two martensitic stainless steels with different Mn content. Particularly, the presence of reactions competing for the carbon and the influence of manganese/chromium bands was experimentally studied. Results are discussed in the context of the applicability of the CCE model to stainless steels.

Materials and experimental methods

The chemical composition of the two medium-carbon stainless steels investigated in this work is given in Table 1. A low-manganese alloy (LMn) containing 0.31 wt% C and 0.77 wt% Mn and a high-manganese alloy (HMn)

Table 1. Chemical composition of the steels, in wt%.

Alloy	C	Mn	Si	Cr	Ni	Al	N	Fe
LMn	0.31	0.77	0.3	13.1	0.20	0.005	0.03	balance
HMn	0.32	3.00	0.3	13.1	0.20	0.002	0.03	balance

containing 0.32 wt% C and 3.00 wt% Mn, keeping the concentration of all other alloying elements the same. Steel ingots were cast by Acerinox and further processed in RINA-CSM. After homogenisation at 1270°C for 3 h, the material was hot-rolled with the last pass at 1000°C and cooled down to RT at a rate of 0.1°C/s, leading to $100 \times 20 \times 2$ cm^3 slabs. Subsequently, an annealing treatment was performed at 600°C for 24 h to soften the material.

Cylindrical specimens with 10 mm in length and 4 mm in diameter were machined by electron discharge machining (EDM) from the slabs with the long axis parallel to the rolling direction. Heat treatments were applied with a DIL805 D Bähr/TA dilatometer to obtain different Q&P microstructures. The temperature was controlled using an S-type thermocouple that is spot-welded onto the middle of the cylindrical specimens. Two quartz rods were used for clamping and flexible fixing specimens. During the heating and isothermal holding segments, a vacuum of approximately 10^{-4} mbar was maintained in the chamber. Helium was used during the cooling process to control the cooling rate. Figure 1 shows a scheme of the heat treatments applied to the cylindrical specimens in the dilatometer. In the following section, the selection of austenitisation conditions, cooling rate, quenching temperature and partitioning conditions will be explained in further detail. Selected heat treatments were applied ending at temperatures below RT for a better observation of martensite kinetics and possible determination of the Ms temperature corresponding to fresh martensite in the last quench. The heat treatments that were considered for this additional investigation will be mentioned in Analysis of dilatometry curves section as they are needed in the argumentation. These "sub-zero" heat treatments were also applied in the same dilatometer.

After heat treatment, the specimens were cut in half, and the surfaces were prepared for metallographic analysis. Firstly, they were ground using P800, P1000, P1200 and P2000 abrasive papers. Next, they were polished with 3 μm and 1 μm diamond paste. Finally, samples were polished with an OPS suspension for 15 min and then washed with soap to remove the OPS stains and ultrasonically cleaned in isopropanol for 10 min. To reveal the microstructure, a Vilella reage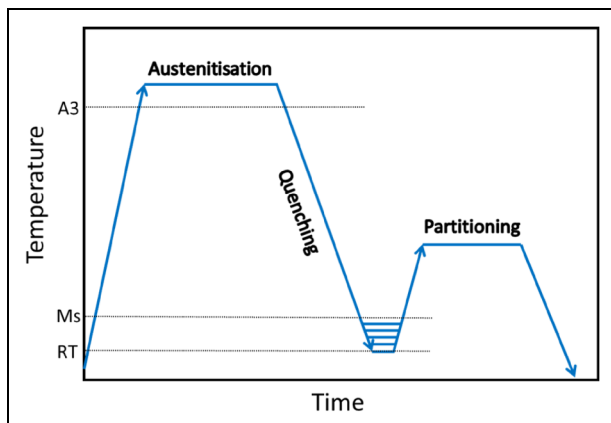nt consisting of 1 g picric acid, 5 ml HCl and 100 ml ethanol was applied. This solution outlines the carbides and etches the martensite. The etched microstructures were analysed by light optical microscopy (LOM) and with a field emission gun scanning electron microscope (FEG-SEM, JEOL JSM-6500F) operating at 15 kV and 10 mm working distance.

To evaluate the degree of carbon partitioning, the volume fraction and carbon concentration of austenite after Q&P treatment were evaluated by X-ray diffraction (XRD) experiments in a Bruker D8-Advance diffractometer, in which the phase constituents and the austenite lattice parameter at RT were measured. Diffraction angles in the range of $45° < 2\theta < 130°$ were measured with Co Kα radiation, using a step size of 0.035° 2θ with a counting per step of 4 s. This 2θ range covers the (110), (200), (211), (220) martensite peaks and the (111), (200), (220), (311) austenite peaks. The carbon concentration within the RA was calculated from its lattice parameter a. Since there is no specific empirical formula developed for Q&P processed stainless steels,[34] we chose two commonly used empirical formulas equation (1)[34] and equation (2)[37] for comparison:

$$\begin{aligned} a(\text{nm}) = {} & 0.3578 + 0.0033 \text{ wt\%C} + 0.000095 \text{ wt\%Mn} \\ & - 0.00002 \text{ wt\%Ni} + 0.00006 \text{ wt\%Cr} \\ & + 0.00056 \text{ wt\%Al} + 0.00031 \text{ wt\%Mo} \\ & + 0.00018 \text{ wt\%}V \end{aligned}$$

$$\tag{1}$$

$$\begin{aligned} a(\text{nm}) = {} & 0.3556 + 0.00453 \text{ wt\%C} + 0.000095 \text{ wt\%Mn} \\ & - 0.00002 \text{ wt\%Ni} + 0.00006 \text{ wt\%Cr} \\ & + 0.00056 \text{ wt\%Al} + 0.00031 \text{ wt\%Mo} \\ & + 0.00018 \text{ wt\%V} \end{aligned}$$

$$\tag{2}$$

Electron probe microanalysis (EPMA) was performed with a JEOL JXA 8900R microscope to quantify elemental segregation using an electron beam with an energy of 10 keV and beam current of 100 nA employing wavelength dispersive spectrometry. The composition at each analysis location of the sample was determined using the X-ray intensities of the constituent elements after background correction relative to the corresponding intensities of reference materials. The obtained intensity ratios were processed with a matrix correction program CITZAF.[38]

Design of heat treatments

Austenitisation conditions and cooling rate

According to thermodynamic calculations performed, 1100°C is a temperature sufficiently high to ensure the dissolution of all precipitates in both alloys. However, related literature[19–21] shows that the annealing time for full austenitisation is longer in martensitic stainless steels than that in carbon steels due to the low diffusion of Cr in ferrite. As a result, austenitisation conditions of 1100°C for 15 min were employed in the present work.

Figure 1. Applied Q&P heat treatments on LMn and HMn alloys.
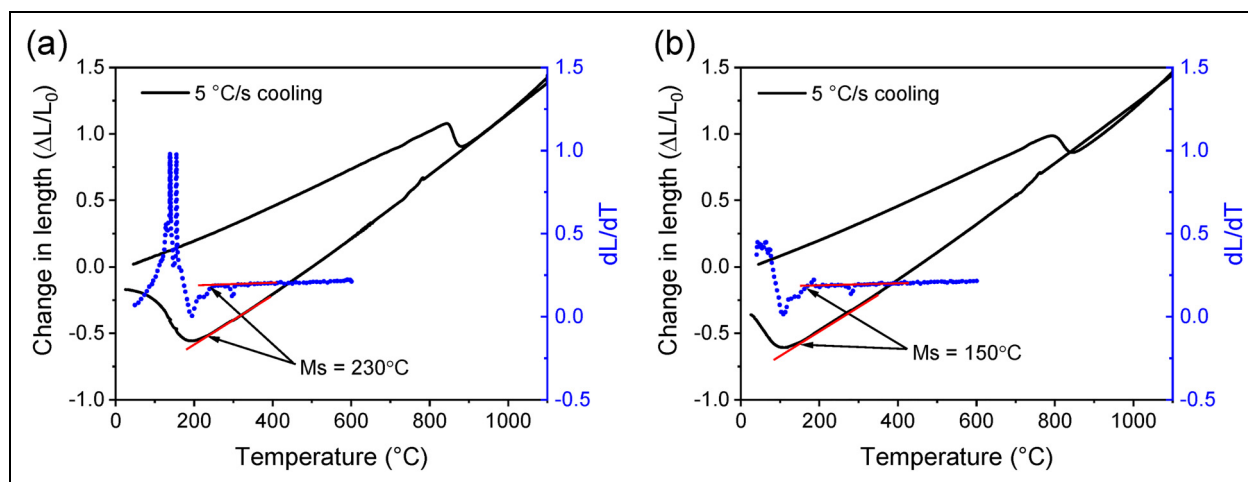
Figure 2. Dilatometry curves of change in length versus temperature (continuous line) and corresponding change in slope (dotted line) during Q&P treatment for (a) alloy LMn and (b) alloy HMn. The arrows point to the drop in the differential curves, indicating the start temperatures of the martensitic transformation.

The dependence of the martensite start temperature on the cooling rate was investigated for both LMn and HMn alloys. Specimens were subjected to austenitisation at 1100°C for 15 min, followed by cooling at rates of 5°C/s, 10°C/s, 20°C/s and fast quench. The dilatometry curves did not show any difference in Ms temperature. So only one curve corresponding to cooling at 5°C/s is shown in Figure 2. The instabilities observed in dilatometry curves at around 800°C are due to the cooling gas pumping into the chamber during quenching.

For better visualisation of the martensite formation kinetics, differential curves around the Ms temperature in the cooling section are included as dashed lines. The initiation of the martensite transformation during cooling is indicated by a drop in the differential curve. In Figure 2(a), for alloy LMn, the measured M_S temperature is 230°C, while the most rapid transformation kinetics are observed at 200°C. In Figure 2(b), for alloy HMn, the M_S is at 150°C, and the quickest transformation kinetics occur at 100°C. It is noteworthy that, in both alloys, prior to reaching the M_S temperature during cooling, there are slight fluctuations on the differential curves. These fluctuations manifest as gradual changes in the dilatometry curves, suggesting the possibility of a minor presence of previously transformed martensite with a higher M_S temperature, potentially due to microstructural or chemical heterogeneities. The transformation is not completed in any of the alloys at RT.

Considering the experimental observations, a cooling rate of 5°C/s was selected for all experiments. This cooling rate allows better control of the microstructure development and a reliable M_S temperature measurement.

Characterisation of martensite formation and selection of quenching temperatures

In order to obtain appropriate quenching temperatures for the formation of controlled fractions of martensite, it is necessary to carefully determine the martensite transformation kinetics. This is achieved by relating dilatometry curves showing martensite formation with kinetic curves showing martensite fraction. For this purpose, the thermal expansion coefficient (CTE) of austenite and martensite and the fraction of martensite present at RT must be known.

The CTE of austenite was obtained from the slope of the change in length versus temperature observed during cooling from the austenitisation conditions and before martensite forms. To measure the CTE of martensite, specimens quenched at 5°C/s were placed into liquid nitrogen for 20 min to form a near-fully martensitic structure. While not all of the austenite transformed during the liquid nitrogen treatment, the very small amount that remained was assumed to have a negligible effect on the thermal expansion of martensite. Subsequently, these specimens were reheated in a dilatometer at a rate of 10°C/s to 350°C. Under these reheating conditions, microstructural tempering was not expected, ensuring that the thermal expansion of martensite during reheating was solely influenced by temperature changes and excluded the possibility of carbon content variation. The measured slope of the change in length versus temperature during reheating allowed the calculation of the CTE of martensite. The XRD measurements conducted allowed us to determine the volume fractions of martensite present at RT, resulting in values of 0.89 for alloy LMn and 0.68 for alloy HMn. These determined fractions were subsequently employed in the lever rule calculations.

The experimental results obtained above are plotted together in Figure 3(a) and (b) for alloys LMn and HMn, respectively, with the CTE obtained of martensite (bcc) and austenite (fcc) presented. From this curve, the martensite fraction formed at a given temperature during continuous cooling to RT can be estimated based on the lever rule, leading to the curves presented in Figure 3(c) and (d).

Five quenching temperatures, ranging from RT with 25–30°C increments up to close to the M_S, were selected for precise investigation for each alloy. These selected quenching temperatures and corresponding martensite fractions are
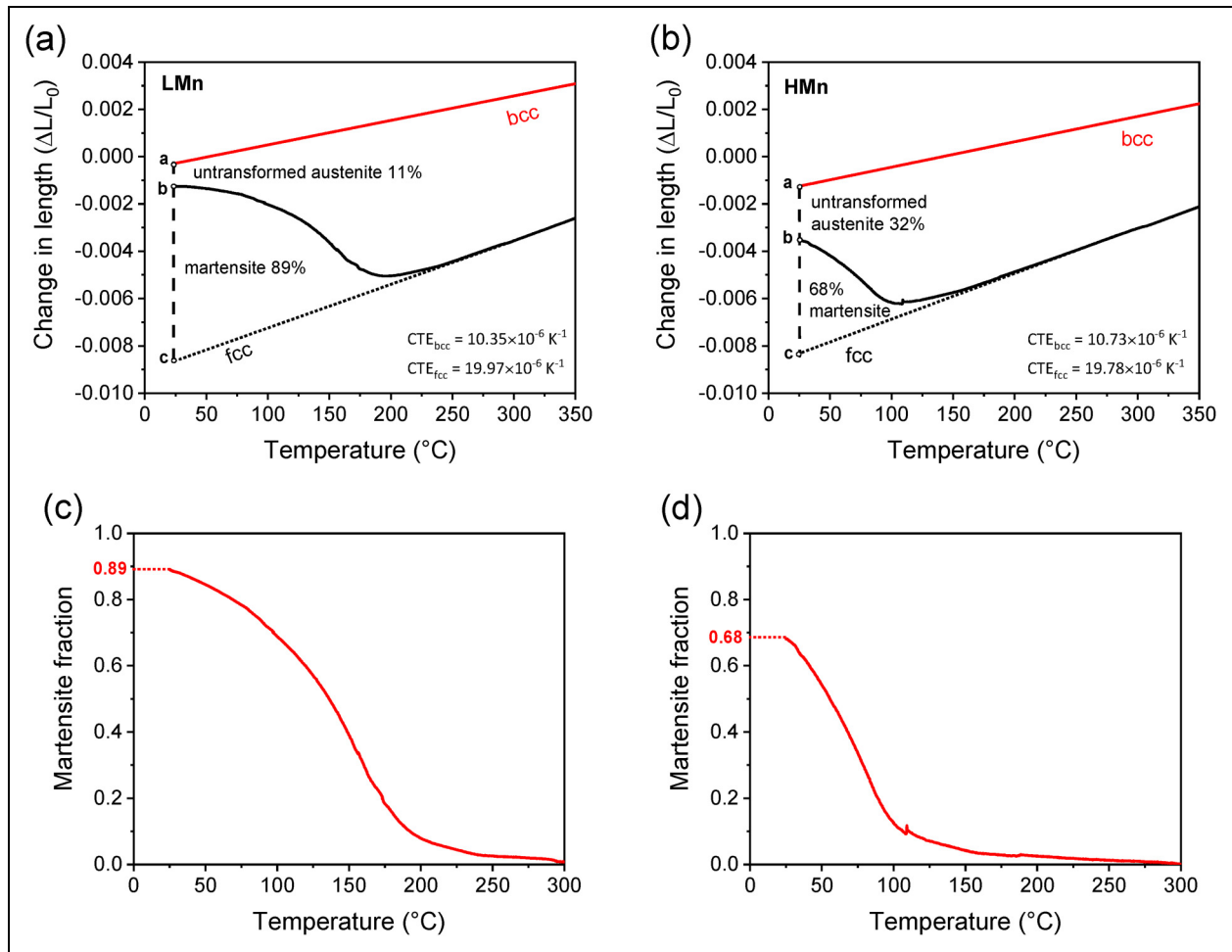
Figure 3. Change in length versus temperature during cooling and reheating and experimental volume fraction of martensite calculated applying lever rule for alloy LMn (a, c) and alloy HMn (b, d), respectively.
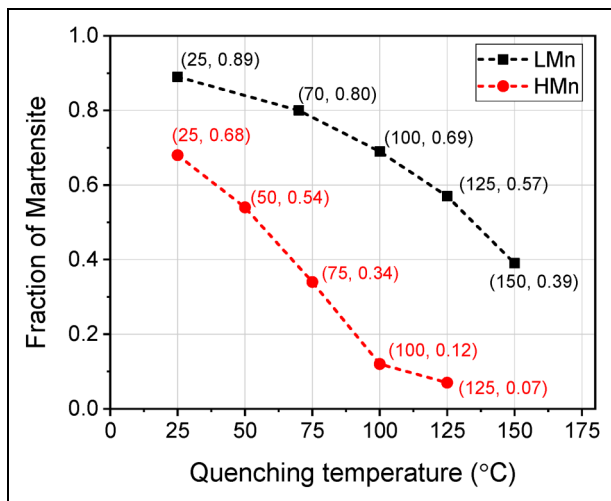
Figure 4. Selected quenching temperatures for Q&P heat treatments and corresponding fraction of primary martensite as determined by the lever rule.

shown in Figure 4. Materials were held at the quenching temperature for 20 s, which is sufficiently long to stabilise the temperature in the specimen without any phase transformation.

Selection of the partitioning conditions

Previous investigations by Mola et al.[34] on the Q&P processing of martensitic stainless steels have shown that after quenching to conditions leading to a fraction of martensite of 0.65, partitioning at 450°C for 3 min was sufficient for full stabilisation of the remaining austenite without fresh martensite formed in the final microstructure. Additionally, the works of Tsuchiyama et al.[19] and Tobata et al.[21] showed that partitioning conditions of 450°C for 10 min leading to a fraction of martensite of 0.80 also allowed significant retention of austenite at RT, although precipitation of M_3C and M_7C_3 types of carbides occurred on the RA/martensite interfaces. Therefore, in the present investigation, partitioning conditions of 450°C for 5 min were selected to maximise carbon partitioning while trying to minimise the precipitation of carbides.

The diffusion distance of carbon within austenite at 450°C for 5 min was evaluated by employing the diffusion coefficient of carbon in austenite, as detailed in reference.[5] The results of this calculation unequivocally demonstrate that under these conditions, carbon can distribute over a distance of 10 μm. Therefore, this condition is sufficient for the partitioning of carbon and the stabilisation of austenite. The heating rate from the quenching temperature to the

partitioning temperature is also 10°C/s. Additionally, the cooling rate after partitioning remains consistent with the initial cooling rate, which is 5°C/s. Since the present work involves different quenching temperatures, it is expected that the competition between carbon partitioning and carbide precipitation will be affected by the fraction of austenite present at the partitioning step.

Results

Analysis of dilatometry curves

Figure 5(a) shows relative length changes versus temperature of LMn samples during the Q&P process. Some of the presented heat treatments ended at sub-zero temperatures. Martensite starts forming at 230°C (Ms1), leading
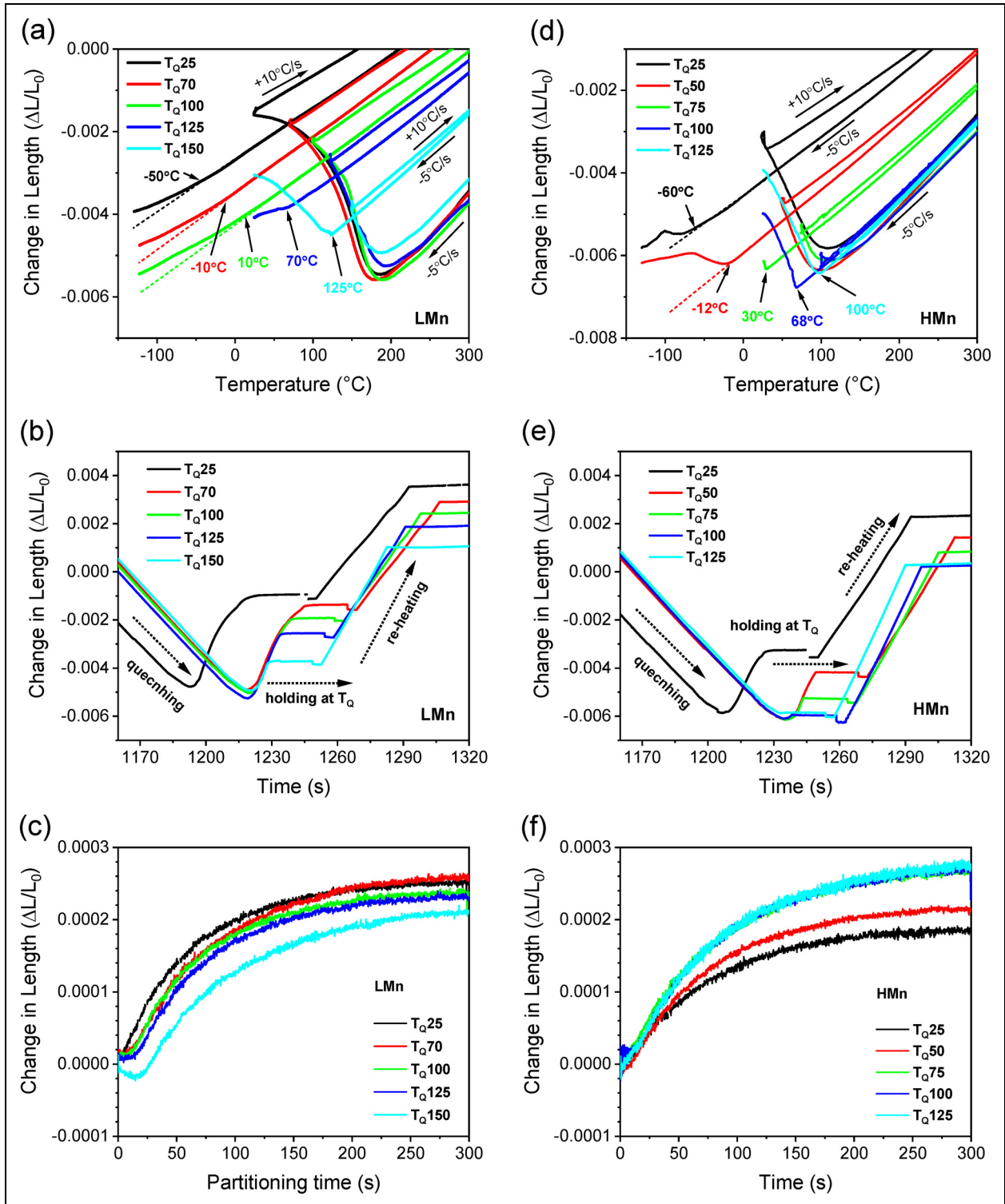
Figure 5. Relative change in length versus temperature during Q&P experiments, versus time during the quenching step followed by reheating, and versus partitioning time during the partitioning step for alloys (a–c) LMn and (d–f) HMn.

to different fractions ranging from 0.89 to 0.39 as a function of the quenching temperatures, as explained in Design of heat treatments section. Specimens are then reheated to the partitioning temperature of 450°C, where the material is held for 5 min. After the partitioning stage, the specimens are cooled to RT, forming fresh martensite at a temperature Ms2 in specimens initially quenched to 125°C (Ms2 = 70°C) and 150°C (Ms2 = 125°C). When the final quench was down to −120°C, the formation of fresh martensite was observed in the dilatometry curves of specimens initially quenched to 25°C (Ms2 = −50°C), 70°C (Ms2 = −10°C) and 100°C (Ms2 = 10°C).

Figure 5(b) shows the change in length versus time during the quenching and reheating stages for alloy LMn. The 20 s holding at T_Q does not show any sign of phase transformation. The changes in the CTE displayed in the reheating stage for different specimens correspond to the differences in phase fractions, that is, the lower the fraction of martensite formed in the first quench (M1), the higher the expansion coefficient. The change in length observed during the partitioning step depends on the quenching conditions, as shown in Figure 5(c). In the case of quenching to 25°C, a continuous expansion is observed. For specimens quenched to 70°C, 100°C and 125°C, a stable length is registered during the first 10 s before expansion. In the case of quenching to 150°C, a slight contraction during the first 20 s is observed before expansion.

In the case of alloy HMn, as shown in Figure 5(d), fresh martensite formed during the last quenching step in specimens quenched to 75°C (Ms2 = 30°C), 100°C (Ms2 = 68°C) and 125°C (Ms2 = 100°C). When the final quench was down to −120°C, the fresh martensite was also observed after quenching to 25°C and 50°C and the Ms2 was −60°C and −12°C, respectively. As displayed in Figure 5(e), similar to LMn alloy, no phase transformation was observed during the reheating stage. All specimens exhibit continuous expansion during the partitioning process, as shown in Figure 5(f). The expansion is in all cases of an extent of less than 0.03%, which can be associated to the homogenisation of thermal gradients and the process of carbon partitioning. This expansion has already been reported in a couple of published articles[4,9,11,29,35] in which similar graphs are shown.

Phase fractions

Figure 6(a) and (b) shows the phase fraction after each Q&P treatment for both alloys. The volume fraction of RA was measured by XRD as shown in Figure 6(c) and (d), while
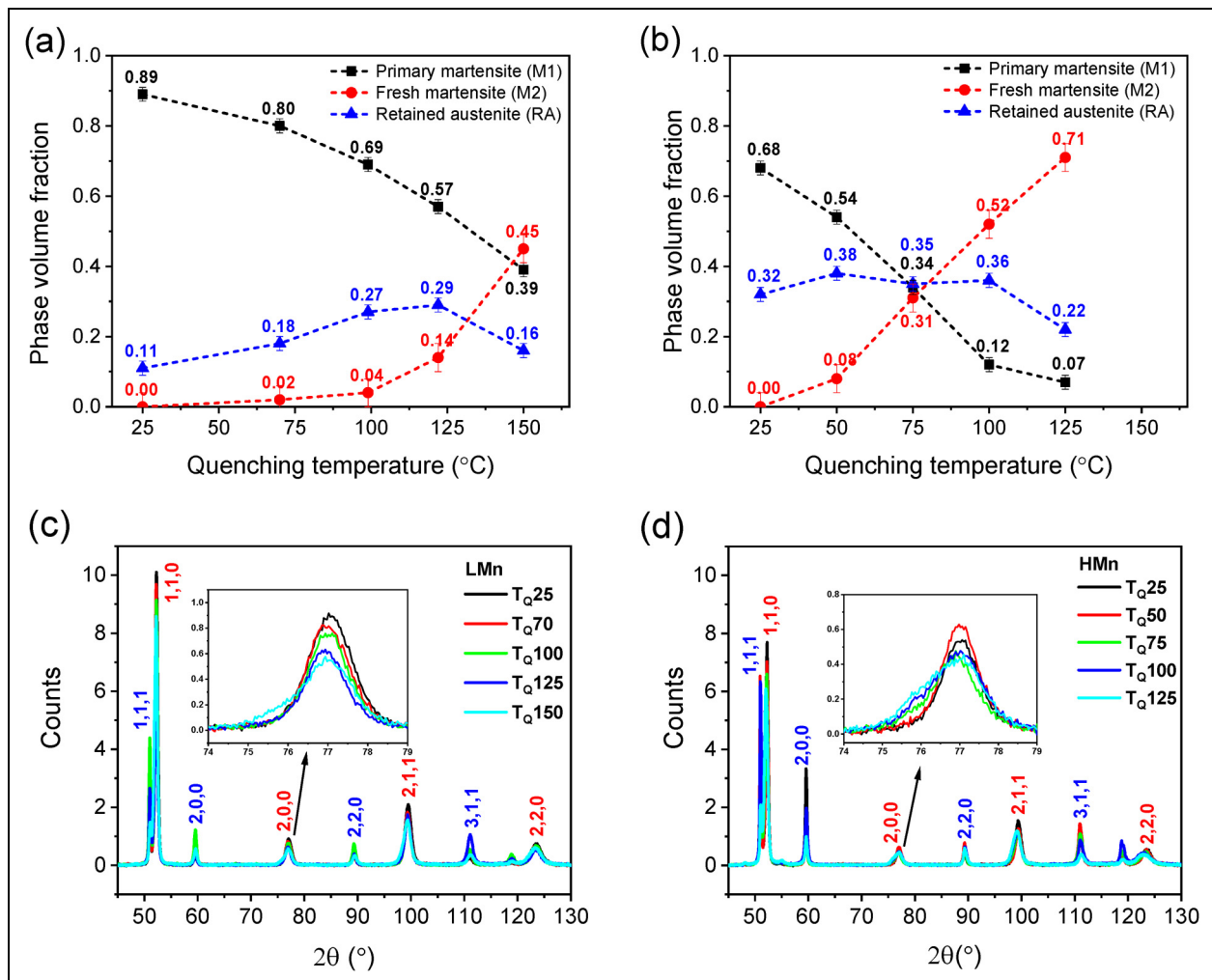
Figure 6. Phase volume fraction (a, b) and XRD patterns (c, d) in Q&P specimens of LMn alloy and HMn alloy, respectively.

the fraction of martensite formed during the quenching step (in the following, M1) was obtained by the lever rule (see Figure 3). The fraction of fresh martensite formed during the last quenching step (in the following, M2) was calculated by phase balance, assuming no transformation of M1. As we can see, some M2 (typically a fraction below 0.08) is obtained by phase balance in specimens in which no expansion was observed during the last quench (to RT). Considering the measurement limitation of ±0.02 error for both primary martensite and RA, the fresh martensite will have ±0.04 error bar to the calculated values. In the dilatometer, such a small amount of fresh martensite cannot be obtained with sufficient accuracy.

As shown in Figure 6(c), the XRD spectrum for LMn alloy only shows martensite (peaks marked by red index) and austenite (peaks marked by blue index) for all treated specimens. With increasing quenching temperature, martensite peaks gradually become less symmetric and tend to move to low angles, which indicates an increasing presence of fresh martensite (M2). This is further visible in the insert of Figure 6(c), which shows the evolution of the {002} peak of martensite with increasing quenching temperature. Peak splitting occurs when the carbon content of steel is higher than the threshold of about 0.2 wt%, often quoted as the minimum carbon level required for a detectable martensite tetragonality.[34] HMn specimens, Figure 6(d), displays the same martensite and austenite peaks as LMn alloy. Peak splitting was also observed in martensite in this material for quenching temperatures equal to 75°C and higher.

As shown in Figure 6(a), in alloy LMn, the fraction of RA increases from 0.11 after quenching to RT to 0.29 after quenching to 125°C when fractions of fresh martensite higher than 0.14 are observed. At higher quenching temperatures, the fraction of RA does not increase further, although more fresh martensite is formed. A similar trend is observed in alloy HMn as shown in Figure 6(b), but higher fractions of RA were stabilised. The fraction of RA remains approximately constant (0.35–0.38) within measurement error for quenching temperatures between 50°C and 100°C, while the fractions of primary and fresh martensite clearly change in the same range. Then the fraction of RA is reduced to 0.32 and 0.22 at RT and 125°C, respectively.

Microstructure characterisation

*LMn alloy.* Figure 7 shows optical micrographs of alloy LMn specimens after different Q&P treatments. Specimens show heterogeneous microstructures, which probably come from chemical segregation. The etching surface shows two distinct regions, an alternation between the less-etched bright bands and dark etched bands. According to the working mechanism of Vilella etchant, the dark features should correspond to the carbon-depleted martensite, while the bright bands contain RA, probably adjacent to carbon-rich martensite.

The etched microstructural bands show a stronger contrast for lower fractions of primary martensite. This can be seen by comparing Figure 7(a) for the specimen quenched to 70°C with f_{M1} =0.80, Figure 7(b) for the specimen quenched to 125°C with f_{M1} =0.57 and Figure 7(c) for the specimen quenched to 150°C with f_{M1} =0.39, which also corresponds with an increased carbon depletion of the primary martensite. Unfortunately, the LOM images do not allow for a distinction between RA and fresh martensite (M2). This is mainly due to two reasons: (a) the higher carbon content in M2 enhances its etching resistance, leading to similar etching features as RA and (b) etching features are further shaded by the strong contrast of M1 when M1 is volume dominant in the microstructures.

Figure 8 shows SEM micrographs of the same specimens displayed in Figure 7. The carbon-depleted M1 bands now have a brighter contrast under the SEM. Figure 8(a) shows selective dissolution (etching) on localised regions in the specimen quenched to 70°C. The M1-rich bands show more of this localised etching uniformly distributed on the surface. Some discontinuous precipitates were observed inside prior austenite grain boundaries. Figure 8(b) presents the microstructure of the specimen quenched to 125°C, showing that more depletion of M1 leads to more etched M1-rich bands and smoother RA-rich bands. In the specimen quenched to 150°C in Figure 8(c), more precipitates are observed inside the carbon-depleted M1, which was attacked heavier by the etchant.

Two types of precipitates can be observed from the etched locations: (a) small particles located inside M1, probably carbides and (b) lamellar precipitates at prior austenite grain boundaries. The visibility of small particles is dependent on Q&P samples (more frequent in specimens with a higher fraction of M1), while the grain boundary precipitates did not show any specific relationship with the specimen or location.

HMn alloy. The light optical micrographs of Alloy HMn also exhibit banded microstructures, as shown in Figure 9. In this case, there are three kinds of etching
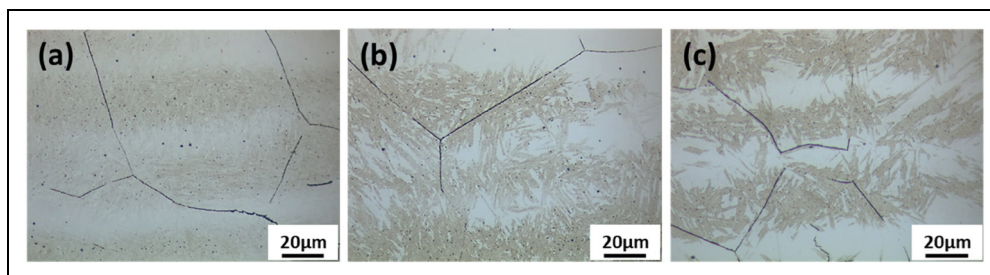
Figure 7. LOM images of LMn Q&P specimen with decreasing volume fraction of M1: (a) specimen quenched to 70°C, (b) specimen quenched to 125°C, (c) specimen quenched to 150°C.
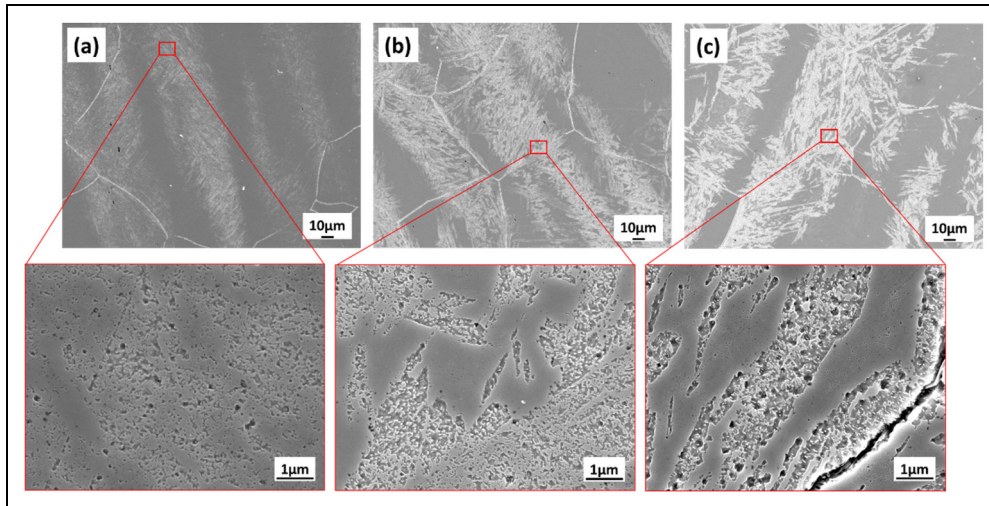
Figure 8. SEM micrographs of LMn Q&P specimen with decreasing volume fraction of M1: (a) specimen quenched to 70°C, (b) specimen quenched to 125°C, (c) specimen quenched to 150°C.
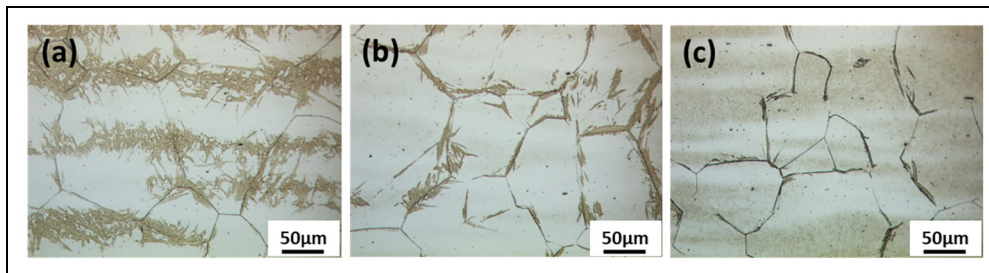
Figure 9. LOM images of HMn Q&P specimen with increasing volume fraction of M2: (a) specimen quenched to 75°C, (b) specimen quenched to 100°C, (c) specimen quenched to 125°C.

features: bright bands (corresponding to higher carbon concentration), dark bands (corresponding to carbon depletion) and bands with an intermediate contrast, such as the ones shown in Figure 9(c). In light of the phase fraction measurements conducted in the preceding sections, it can be inferred that the bands exhibiting intermediate contrast are likely indicative of the presence of fresh martensite, characterised by a higher carbon concentration when compared to primary martensite.

For quenching temperatures in which the final microstructures contain only dark and bright etching features, as shown in Figure 9(a) for the specimen quenched to 75°C, LOM reveals a banded morphology similar to the one observed in alloy LMn specimen quenched to 125°C, but with higher contrast. Within the dark M1 band, some white blocky MA islands remain unetched.
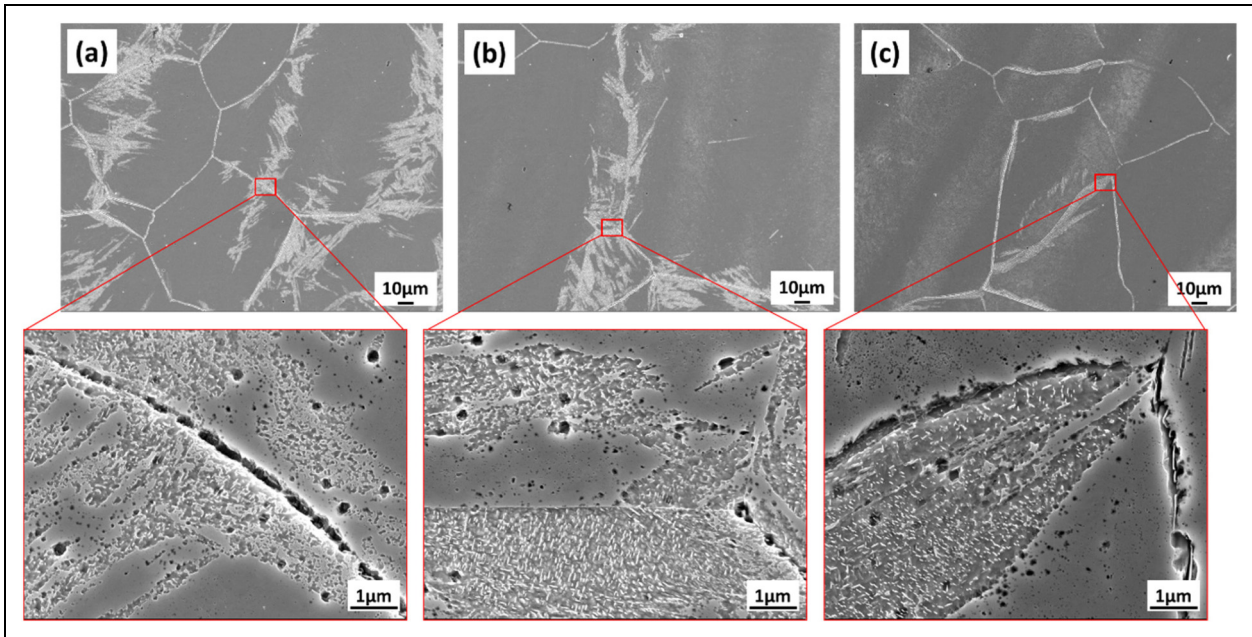
The specimen quenched to 100°C led to a low fraction of M1 (0.12), which was only observed along prior austenite grain boundaries. As can be seen from Figure 9(b), RA is a major phase, which was confirmed with XRD measurements. Fresh martensite (M2) appeared as grey traces, tending to form bands. Figure 9(c) shows the microstructure of the specimen quenched to 125°C. The increased fraction of fresh martensite is shown as significantly thicker grey bands. With a fraction of M1 close to zero, the dark

etching features are only observed along prior austenite grain boundaries.

SEM micrographs in Figure 10 further exhibit the different etching features of M1 and M2 and also reveal the different morphologies of small particles and grain boundary precipitates. M1 bands are deep etched and full of small particles (probably carbides). M2 is shown as a slightly etched coarse surface, which cannot be clearly separated from the RA area.

Grain boundary microstructure. As observed in previous LOM and SEM microstructures, there are precipitates located at the prior austenite grain boundaries and small particles in M1-rich bands (Figures 8 and 10). To understand the precipitation behaviour, the quenched microstructures before partitioning are displayed in Figure 11. The prior austenite grain boundaries contain some precipitates. But no small particles can be observed inside the grains, suggesting that small particles inside grains distributed on M1-rich bands (Figures 8 and 10) are formed in the later partitioning stage. Huang et al.[35] studied the dissolution process of Cr-rich carbides in martensitic stainless steels with a composition of Fe-0.47C-13.1Cr-0.36Mn (wt%) and found that their conditions were sufficient for the full dissolution of Cr-rich carbides. Compared to our designed heat treatment of annealing at 1100°C for 15 min, Cr-rich

Figure 10. SEM images of HMn Q&P specimen with decreasing volume fraction of M1: (a) specimen quenched to 75°C, (b) specimen quenched to 100°C, (c) specimen quenched to 125°C.
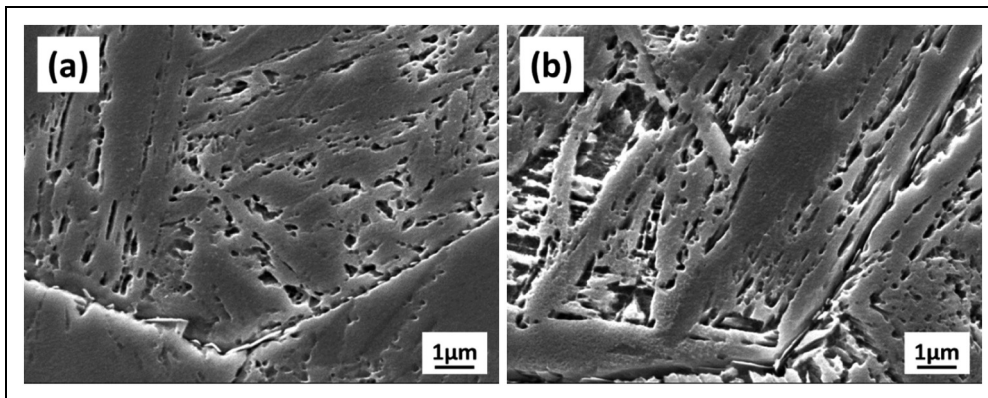
Figure 11. The microstructure observed with SEM of (a) LMn and (b) HMn alloys that were quenched to RT without partitioning processing.

carbides are supposed to be fully dissolute during annealing. Similar carbide morphology at grain boundaries in stainless steels has been identified as $M_{23}C_6$-type Cr carbides in the literature (e.g. see Hu et al.[39]). Thus, the precipitates at prior austenite grain boundaries are most probably Cr carbides ($M_{23}C_6$) that formed during quenching. Cr-carbide precipitation at grain boundaries causes Cr depletion in its surroundings, making these regions more susceptible to etching.

Discussion

Microstructural evolution during Q&P treatments

To better understand the microstructural evolution during the application of the Q&P treatments, experimental results are compared with theoretical outcomes from the CCE model. Assuming that the partitioning process leads to full carbon partitioning from primary martensite into austenite, in the absence of interface migration or competing processes such as carbide precipitation, the balance of carbon at the end of the partitioning process and before the final quench is[3]:

$$f_A \cdot X_C^{A(\mathrm{CCE})} + f_{M1} \cdot X_C^{M1(\mathrm{CCE})} = X_C^{\mathrm{alloy}} \qquad (3)$$

where $f_A, f_{M1}, X_C^{A(\mathrm{CCE})}, X_C^{M1(\mathrm{CCE})}$ are the volume fractions and carbon contents of austenite and primary martensite, respectively, at the end of the partitioning step and X_C^{alloy} is the nominal carbon content of the alloy. Particularly, $X_C^{A(\mathrm{CCE})}$ refers to the carbon in austenite at the end of the partitioning step and assuming full carbon partitioning. For every quenching temperature investigated, the volume fraction of martensite f_{M1} (i.e. the fraction of primary

martensite) at the end of the partitioning stage has been determined through dilatometry, while the fraction of austenite at the partitioning stage is thereby $(1 - f_{M1})$. The f_{M1} fractions are shown in Figure 6.

It follows that the theoretical carbon concentration in austenite $X_C^{A(CCE)}$ at the end of the partitioning step and in the absence of competing reactions can be obtained from equation (3) as:

$$X_C^{A\,(\mathrm{CCE})} = X_C^{\mathrm{alloy}} / (1 - f_{M1}) \qquad (4)$$

The carbon content of austenite at the partitioning step is related to the stability of this phase upon further quench. Therefore, if austenite is sufficiently enriched in carbon, it remains retained at RT. However, if carbon enrichment is not sufficiently high, part (or all) of this austenite will transform into fresh martensite (M2). The observation of an additional Ms on quenching after the partitioning step can be associated to the carbon content of the austenite at the end of the partitioning step. The carbon concentration in the austenite at the end of the partitioning step can be calculated from the experimental Ms2 temperatures shown in Figure 5 using equation (5) developed based on experimental data from references[18–21,34,35] where w_i represents the concentration in weight percentage of the elements identified by the subscript. Please note that Equation (5) does not account for the influence of prior austenite grain size (PAGS) on the Ms temperature. However, our PAGS measurements, conducted using LOM images, have indicated that both alloys fall within a similar range of 103 ± 43 μm. Consequently, we anticipate that there will not be significant error when estimating the Ms temperature attributable to PAGS.

$$\mathrm{Ms}(°\mathrm{C}) = 553.7 - 530.8 w_C - 30.4 w_{\mathrm{Mn}} - 12.1 w_{\mathrm{Cr}}$$
$$(5)$$

Figure 12 compares the carbon concentration of RA experimentally obtained with that calculated with Equation (4) for both alloys. The agreement between the carbon content in austenite calculated assuming CCE conditions ($X_C^{A\,(CCE)}$) and experimentally estimated from Ms2 (X_C^{RA}) is significant, although there is a consistent overestimation of the CCE-based values. This overestimation indicates the presence of competition during the application of the Q&P process that is not considered in the CCE model.

For the case of alloy LMn (Figure 12(a)), the CCE-based values are higher than the estimated from Ms2 for the investigated conditions, which indicates the presence of competing reactions consuming carbon that is not available for partitioning. This means that the precipitation of carbides in the primary martensite through tempering is playing a strong role as a reaction competing for the carbon available for partitioning. Indeed, carbides were clearly observed in microstructures quenched to 125°C ($f_{M1}= 0.57$) (Figure 8), corresponding to an increasing fraction of M1.

For the case of alloy HMn, shown in Figure 12(b), the CCE model meets well the experimental results when the martensite volume fraction is less than 0.54, that is, quenching temperature equals to or higher than 50°C. When the quenching temperature is lower, the gap between experimental and calculated carbon in austenite is higher for the maximum fraction of M1 studied, which is 0.68 (quenching temperature of 25°C). Interestingly, in alloy LMn for a similar fraction of M1 (0.69), the gap between experimental and CCE-based carbon in RA remains of the same order as in alloy HMn.

In the following, we are going to evaluate the carbon content associated to the gap between the carbon in austenite based on CCE and the carbon estimated from Ms2 temperature. We will assume that that missing carbon associated to competing reactions is actually in the form of carbides or segregated within M1. Now, equation (6) takes into account the carbon balance in the material at RT (and not at the partitioning step, as it was the case in equation (3)). In an equation this is:

$$f_A \cdot X_C^{A(\mathrm{CCE})} - f_A \cdot X_C^{RA} = f_{M1} \cdot X_C^{M1} \qquad (6)$$
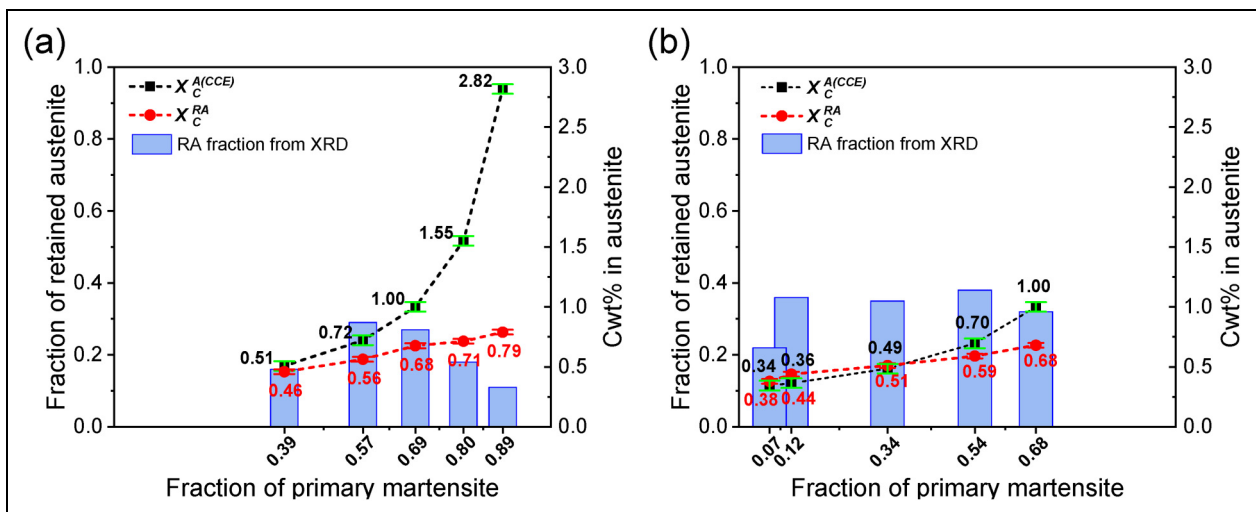
Figure 12. Volume fraction and carbon content of RA versus volume fraction of M1 for (a) LMn alloy, (b) HMn alloy (carbon content from Ms2 with error bar ± 0.02 wt%, carbon content from CCE that calculated based on XRD, with error bar ± 0.04 wt%).
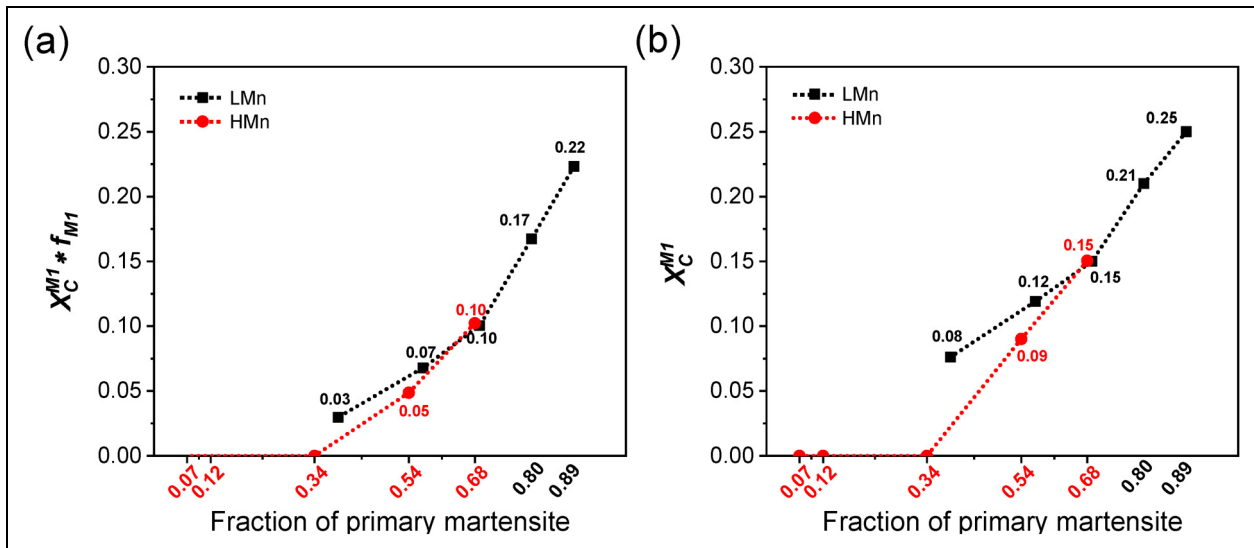
Figure 13. (a) Total carbon content in primary martensite and (b) Carbon concentration in primary martensite versus primary martensite fraction of both alloys.
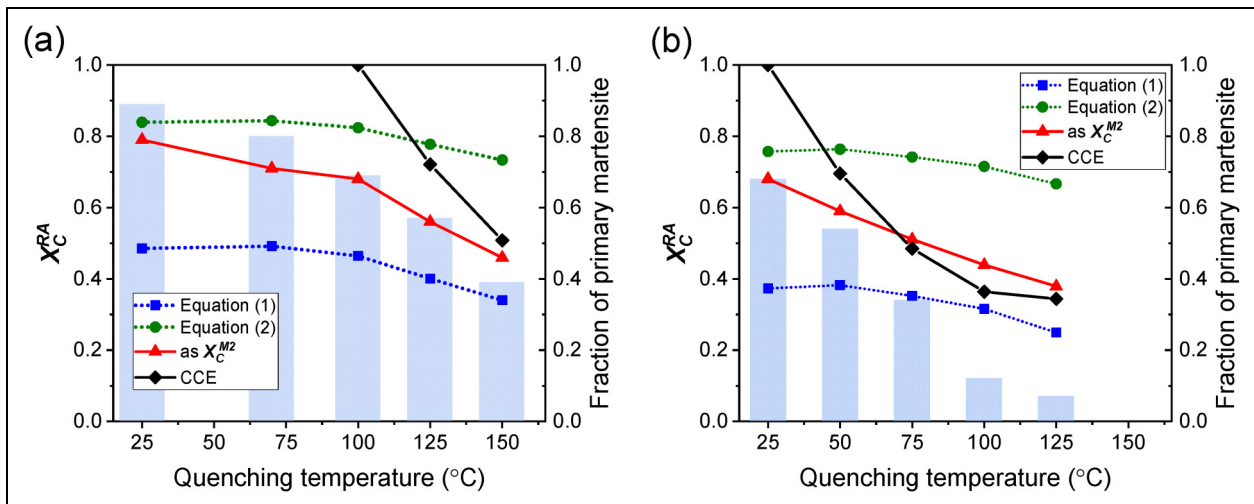
Figure 14. Comparison of carbon concentration in RA obtained by calculations and experiments in both LMn and HMn alloys.

where the X_C^{M1} are the carbon content of primary martensite at real situation. $f_{M1} \cdot X_C^{M1}$ represents the total carbon that does not participate in the process of carbon partitioning to austenite, and it is assumed to remain in the primary martensite. This approach ignores the possibility of carbide precipitation in the RA. In this case, X_C^{RA} refers to the experimentally measured carbon content in RA, which is seen as equal to X_C^{M2}. Applying equation (6), $f_{M1} \cdot X_C^{M1}$ can be calculated. Results are displayed in Figure 13 for both alloys.

Figure 13(a) shows the total carbon content in primary martensite versus the volume fraction of primary martensite. In all the investigated cases, the carbon content in M1 is lower than the alloy's carbon concentration and also lower than that in RA shown in Figure 12. With the primary martensite fraction increasing from 0.34, the carbon trapped in martensite also increased, indicating increased carbide precipitation.

The carbon concentration in primary martensite (in Figure 13(b)) also increases with the increasing fraction of M1 in both alloys. In the LMn alloy, the carbon concentration content increases from 0.08 to 0.25 wt% compared with the 0.31 wt% in the alloy. For the case of HMn alloy, carbon increased from 0 to 0.15 wt%, compared to 0.32 wt% in the alloy. It seems that, the higher the fraction of M1, the higher the density of carbides, which may be associated to a net reduction of martensite/austenite interfaces.[17]

The carbon concentration converted from Ms2 temperature was then compared to the XRD results calculated using two empirical formulas (1)[34] and (2).[37] It can be seen from Figure 14, that the carbon concentration converted from Ms2 temperature falls in the range between equation (1) and equation (2) and equation (2) predicts much higher carbon content than equation (1) for both alloys. In most cases, when the primary martensite fraction is less than

0.70, equation (2) predicts higher carbon concentration than expected according to the CCE model, which implies a carbon content higher than the carbon present in the alloy. On the contrary, equation (1) predicts concentrations of carbon lower than the ones estimated from the M_S2 temperature in several of the investigated conditions, which implies that RA has lower carbon than fresh martensite. Therefore, both equations led to invalid results in the investigated materials.

De Cooman et al.[34] have compared both equations and declared that equation (1) is more reasonable for Q&P stainless steels as it does not exceed the CCE model. This is also applicable for our case, while the problems associated to equations (1) and (2) may be associated to the range of applicability of these equations when they were proposed and further investigation is needed.

As discussed, the presence of carbide precipitation in M1 has been deduced from the carbon balances. SEM images in Figures 8 and 10 showed carbides with two different morphologies, intragranular carbides and grain boundary precipitates. $M_{23}C_6$ precipitates at RT were suspected in Figure 11, the quenched microstructure before partitioning. Similar research results were obtained in Q&P-treated ferritic stainless steels.[40]

The presence of Cr-carbides at prior austenite grain boundaries leads to carbon depletion in their surroundings, which implies a local increase in the Ms temperature at these sites. This explains the formation of martensite only at prior austenite grains shown in Figure 9 for the specimen HMn quenched to 125°C, where only 0.07 volume fraction of M1 transformed all at grain boundaries.

Martensite transformation kinetics

The Koistinen–Marburger equation[8] (in the following, K-M equation) is a general equation describing the progress of transformation from austenite to martensite in carbon steels. During cooling, the austenite-martensite transformation begins at a certain temperature designated as the Ms temperature and proceeds only upon continuous cooling below this temperature. The K-M equation describes the formation of martensite as a function of the undercooling as follows:

$$f_{M1} = 1 - \exp[-\alpha_m \cdot (T_{KM} - T)] \quad (7)$$

where T_{KM} is the K-M martensite start temperature, which is, in general, reportedly lower than the experimentally measured Ms temperatures (e.g. see references[41,42]). T represents any temperature below the T_{KM} at which martensite forms and α_m is a rate parameter that can be calculated based on the chemical composition using the empirical equation (8) proposed by Van Bohemen:[43]

$$\alpha_m = 0.0224 - 0.0107w_C - 0.0007w_{Mn}$$
$$- 0.00005w_{Ni} - 0.00012w_{Cr} - 0.0001w_{Mo} \quad (8)$$

The application of the K-M equation to the present steels leads to the results plotted in Figure 15, together with experimental results from the application of the Lever rule in Figure 3. The experimental Ms temperatures have been employed as "T_{KM}" temperatures, which in general, are considered to be a good first approach. As can be seen, the theoretically deduced martensite kinetics does not fit the experimental results. Not only is the T_{KM} overestimated by using the Ms temperature (as expected), but also the transformation rate α_m was overestimated by equation (8).

In order to understand the reasons for these deviations, the T_{KM} and α_m parameters have been fitted based on the experimental results, as shown in Figure 15. Now, the K-M model fits experimental results well in most parts. However, the early stages of martensite transformation cannot be adequately predicted. The deviation between the experimental kinetics and the K-M fit (Ms-T_{KM}) is 43°C in LMn alloy and 47°C in HMn alloy. This reveals that the formation of the martensite fraction corresponding to T_{KM} temperature (approximately 0.10 for both alloys) takes a longer time than predicted by the K-M model.[44] This effect is known as the "slow-start" phenomenon, and
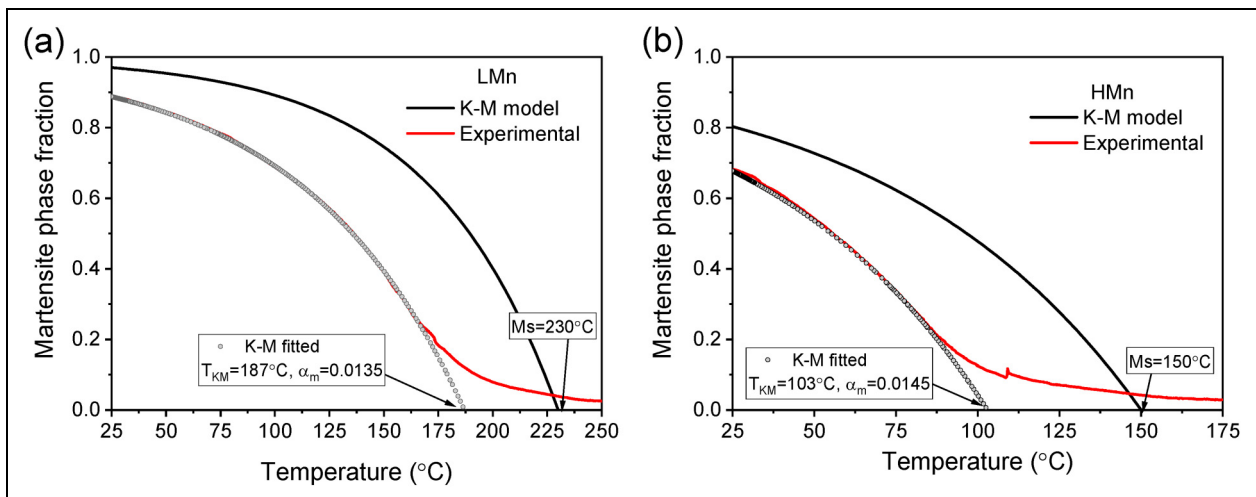
Figure 15. Martensite transformation kinetics built from the K-M model and lever rule for both alloys.

it is attributed to the dispersion of Ms temperatures arising from local chemical inhomogeneities.[45] This means that also, in the present steels, chemical segregation is playing a role in the development of the microstructures during the quenching step, with effects on the partitioning step, as will be evaluated in the following section.

Influence of elemental segregation on microstructures

As discussed, the application of the K-M model to the martensite kinetics has shown that elemental segregation is affecting the microstructure development in the present steels. That was already expected from the optical microscopy graphs shown in Figures 7 and 9. Chemical

segregation originated from the cast and solidification process and can only be eliminated through very long annealing treatments that are often not industrially feasible.[29]

To further understand the effect of chemical segregation on the microstructure development, local EPMA line measurements perpendicular to the observed bands were performed on alloys LMn and HMn at the quenched state. Results are shown in Figure 16 and Table 2. Figure 16(a) and (b) shows the elemental profile of alloys quenched to RT ($T_Q = 25$) before partitioning. Here only the segregating elements are displayed. Particularly, LMn alloy is displayed together with an etched optical microstructure to assist in understanding the correspondence between etching morphology and segregations.
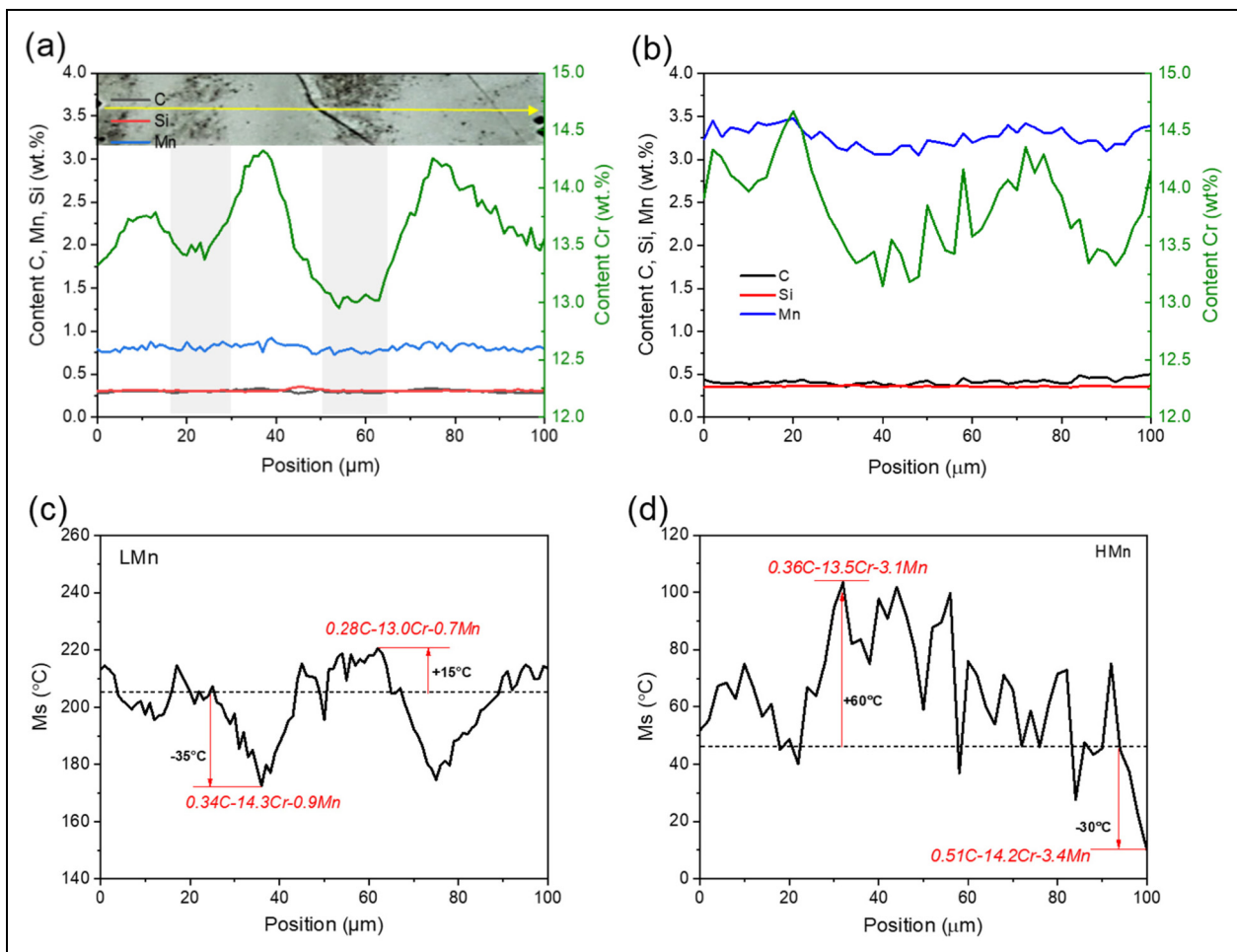
Figure 16. (a–b) Elemental profiles in two regions of both alloys after quenching to RT ($T_Q = 25$) and before partitioning and (c–d) local Ms temperatures calculated based on the local elemental profiles (a, c) LMn alloy and (b, d) HMn alloy.

Table 2. Chemical segregation and Ms temperature in alloying rich and poor bands.

Segregation	C		Cr		Mn		Ms (°C)	
LMn	0.30	+13.3%	13.5	+5.9%	0.8	+12.5%	205	−35
		−6.7%		−3.7%		−12.5%		+15
HMn	0.45	+13.3%	14.0	+1.4%	3.3	+3.0%	42	−30
		−20.0%		−3.6%		−6.0%		+60
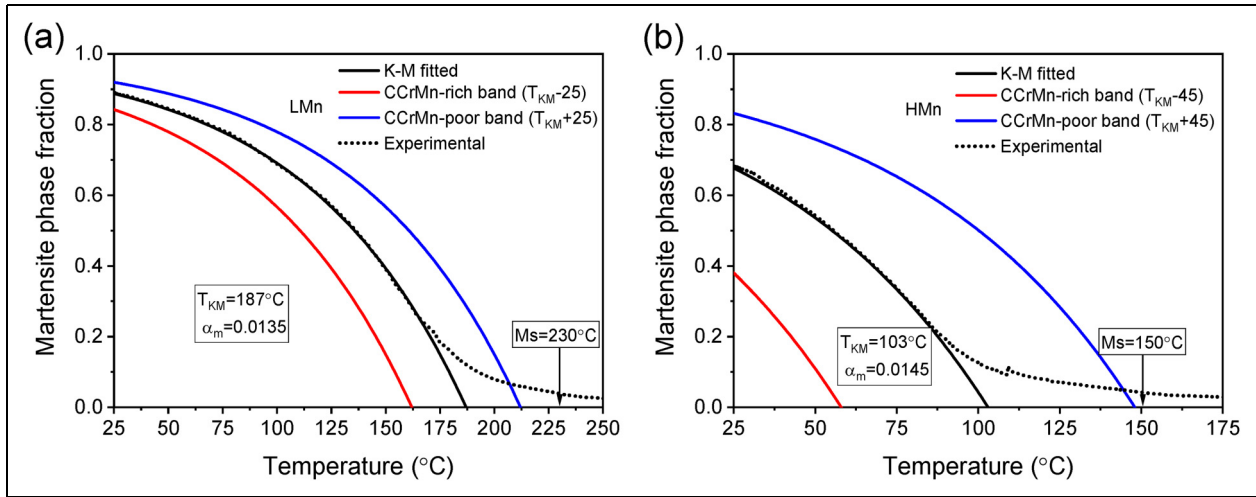
Figure 17. Martensite transformation kinetics at segregation bands of (a) LMn alloy, (b) HMn alloy.

As marked in Figure 16(a), dark bands correspond to an area with lower C, Cr and Mn content, while the brighter bands correspond to higher C, Cr and Mn content; this explains why we observed different bands in optical microscopy. For both alloys, the amplitude of the segregation varies per alloying element. The average chemical composition measured by EPMA was summarised in Table 2, together with the segregation peaks in concentration converted to a percentage for both alloys. Compared with the alloy's composition in Table 1, the measurement of carbon shows the highest deviations. The average content of Cr and Mn is also higher than the general composition, and the segregation content (as indicated in Figure 16(c) and (d)) is more significant in HMn alloy than that in LMn alloy.

In previous section, equation (5) and Figure 14, when we evaluated carbon content in M2 through the Ms2 temperature, Cr and Mn were seen as global content without considering segregation. Table 2 reveals that it is important to account for the influence of chemical segregation of Cr and Mn. The assessment conducted in this context reveals a maximum carbon content difference of 0.05 wt% (with an error bar of $\pm 0.025\%$) between the austenite at alloy-rich and alloy-poor bands. It is noteworthy that such a small margin of error is unlikely to have a significant impact on the conclusions drawn in the previous section.

Figures 16(c) and (d) are local Ms temperatures that were calculated using equation (5) according to the composition shown in Figures 16(a) and (b), respectively. The dash lines in both local Ms graphs represent the Ms temperature of the averaged local compositions. Together with the extreme Ms corresponding to the highest and lowest segregation in each graph was also summarised in Table 2.

Figure 16(c) shows the effect of the changes in composition on the local Ms temperatures across the different bands in alloy LMn. Results indicate significant variations in the local Ms temperatures. Particularly, variations in carbon content seem to be the most relevant in the determination of local Ms temperatures, as can also be seen from equation

(5). Compared to the Ms calculated based on averaged local composition, the local Ms varies from −35 to +15°C from the alloy-rich locations to the alloy-poor locations. These variations will further influence the martensite transformation, leading to a higher presence of primary martensite in alloy-poor bands than in alloy-rich bands.

For the case of alloy HMn, as shown in Figure 16(d), the segregating elements contribute to a 30°C lower Ms in the alloying-rich band and 60°C higher Ms in alloying-poor bands with respect to the average Ms corresponding to that local measurement.

As can be seen, carbon is the most influential element, followed by Mn and Cr. The employed equation for the calculation of Ms (equation (5)) allows to quantify of the effect of elements on the scatter of the averaged Ms.

As discussed above, chemical segregation leads to alloying-rich and alloying-poor bands that have different Ms temperatures. Therefore, the martensite formation kinetics will be different among bands. To assess the differences in the martensite formation kinetics in different bands and its influence on the experimentally measured martensite formation kinetics, the K-M model is used as follows. The scatter data of Ms temperature in Table 2 is considered as scatter for T_{KM} at different bands, leading to ± 25°C for alloy LMn and ± 45°C for alloy HMn. The α_m parameter fluctuates with local compositions in the range of ± 0.0005 among bands, which leads to a minor effect on the calculations. Therefore, for the α_m parameter at different bands, we use the same value that was fitted from Figure 15, that is, 0.0135 for alloy LMn and 0.0145 for alloy HMn. The kinetics of martensite formation is then calculated at different bands leading to the results shown in Figure 17.

During cooling below the Ms temperature, the formation of martensite starts in alloy-poor bands in alloy LMn. When alloy-rich bands start forming martensite, there is already more than 40% martensite on alloy-poor bands. For alloy HMn, martensite starts forming on the alloy-poor band as well. But the phase transformation will differ significantly in alloy-rich bands due to a 90°C lower martensite transformation temperature. For example, alloy-rich bands will

contain 60% less martensite than alloy-poor bands when quenched to 68°C. The T_{KM} temperatures of the alloy-poor band are closer or identical to the experimental measured Ms temperatures.

The EPMA measurement is local; therefore, over the entire surface, there might be locations with a bit higher or a bit lower alloy content than we currently measure. Nevertheless, the local martensite transformation kinetics can be established by fitting the K-M model with local elemental composition and Ms temperatures.

Different phase transformations on bands lead to primary martensite-rich structure on alloy-poor bands and primary martensite-poor structure on alloy-rich bands. After partitioning, the primary martensite-rich band will contain more carbides precipitation, showing as dark etching bands, as revealed by Figures 7–10. While the primary martensite-poor band will stabilise less RA, causing fresh martensite transformation, showing as grey etching bands, as revealed in Figure 9.

Conclusions

We investigated the microstructure evolution of Q&P-treated martensitic stainless steels, with special attention to the applicability of the CCE model and martensitic transformation kinetics with the existence of heterogeneous microstructure. The main conclusions are summarised as follows.

- Phase fractions of primary martensite, RA and fresh martensite have been evaluated based on dilatometry and X-ray diffraction measurement, leading to consistent dependencies with Q&P heat treatment parameters. It has been found that the carbon content in austenite at the partitioning temperature is best estimated based on the experimental measurement of the martensite start temperature corresponding to fresh martensite, which can be determined using sub-zero quench treatments in the dilatometer. Calculations of carbon in RA based on measurements of the lattice parameter using two different equations often used in the literature lead to invalid results in the present alloys.
- The carbon concentration in austenite after the partitioning step calculated assuming full carbon partitioning from martensite to austenite overestimates the actual carbon enrichment observed in austenite. This is due to the precipitation of carbides, including precipitates at prior austenite grain boundaries that formed during the first quenching and small particles inside tempered martensite grains that formed during partitioning. These precipitates consume carbon that is no longer available to partition into austenite.
- The general Koistinen–Marburger parameters were fitted according to the experimental results of martensite kinetics, assisted by local EPMA analysis. It was found that martensite transformation kinetics at alloy-poor and alloy-rich bands differ. The "slow-start" phenomenon was confirmed and explained based on chemical segregation.

- The increasing addition of Mn and its chemical segregation leads to a larger heterogeneity of carbon in alloy HMn. This further leads to a larger Ms temperature scatter between bands in the microstructure of alloy HMn (scatter of 90°C) compared to alloy LMn (scatter of 50°C).

References

1. Speer JG, Streicher AM, Matlock DK, et al. Quenching and partitioning: a fundamentally new process to create high strength trip sheet microstructures. In: *Austenite formation and decomposition*. Warrendale, PA: ISS/TMS, 2003, pp. 505–522.
2. Speer JG, Matlock DK, De Cooman BC, et al. Carbon partitioning into austenite after martensite transformation. *Acta Mater* 2003; 51: 2611–2622.
3. Speer JG, Rizzo F, Matlock DK, et al. The "quenching and partitioning" process: background and recent progress. *Mater Res* 2005; 8: 417–423.
4. Ayenampudi S, Celada-Casero C, Sietsma J, et al. Microstructure evolution during high-temperature partitioning of a medium-Mn quenching and partitioning steel. *Mater* 2019; 8: 100492.
5. Nishikawa AS, Santofimia MJ, Sietsma J, et al. Influence of bainite reaction on the kinetics of carbon redistribution during the quenching and partitioning process. *Acta Mater* 2018; 142: 142–151.
6. Nishikawa AS, Miyamoto G, Furuhara T, et al. Phase transformation mechanisms during quenching and partitioning of a ductile cast iron. *Acta Mater* 2019; 159: 1–16.
7. De Knijf D, Petrov R, Föjer C, et al. Effect of fresh martensite on the stability of retained austenite in quenching and partitioning steel. *Mater Sci Eng A* 2014; 615: 107–115.
8. Koistinen DP and Marburger RE. A general equation prescribing the extent of the austenite-martensite transformation in pure iron-carbon alloys and plain carbon steels. *Acta Mater* 1959; 7: 59–60.
9. Kumar S and BratSingh S. Evolution of microstructure during the "quenching and partitioning (Q&P)". *treatment. Mater* 2021; 18: 101135.
10. Zhang JZ, Dai ZB, Zeng LY, et al. Revealing carbide precipitation effects and their mechanisms during quenching-partitioning-tempering of a high carbon steel: experiments and modeling. *Acta Mater* 2021; 217: 117176.
11. Ebner S, Suppan C, Stark A, et al. Austenite decomposition and carbon partitioning during quenching and partitioning heat treatments studied via in-situ X-ray diffraction. *Mater Des* 2019; 178: 107862.

12. Gao PF, Liang JH, Chen WJ, et al. Prediction and evaluation of optimum quenching temperature and microstructure in a 1300 MPa ultra-high-strength Q&P steel. *J Iron Steel Res Int* 2022; 29: 307–315.

13. Li JY, Xu YB, Lu B, et al. Improvement of strength-ductility combination in ultra-high-strength medium-mn Q&P steel by tailoring the characteristics of martensite/retained austenite constituents. *J Mater Res Technol* 2022; 18: 352–369.

14. Castro Cerda FM, Hernández EI, Ros-Yanez T, et al. Isothermal phase transformations in a low carbon steel during single and two-step partitioning. *Metall Mater Trans A* 2020; 51: 1506–1518.

15. Li Y, Chen S, Wang CC, et al. Modelling retained austenite in Q&P steels accounting for the bainitic transformation and correction of its mismatch on optimal conditions. *Acta Mater* 2020; 188: 528–538.

16. Dai ZB, Ding R, Yang ZG, et al. Elucidating the effect of mn partitioning on interface migration and carbon partitioning during quenching and partitioning of the Fe-C-Mn-Si steels: modeling and experiment. *Acta Mater* 2018; 144: 666–678.

17. Yuan L, Ponge D, Wittig J, et al. Nanoscale austenite reversion through partitioning, segregation and kinetic freezing: example of a ductile 2 GPa Fe–Cr–C steel. *Acta Mater* 2012; 60: 2790–2804.

18. Huang QL, Schröder C, Biermann H, et al. Influence of martensite fraction on tensile properties of quenched and partitioned (Q&P) martensitic stainless steels. *Steel Res Int* 2016; 87: 1082–1094.

19. Tsuchiyama T, Tobata J, Tao T, et al. Quenching and partitioning treatment of a low-carbon martensitic stainless steel. *Mater Sci Eng A* 2012; 532: 585–592.

20. Lu SY, Yao KF, Chen YB, et al. Effect of quenching and partitioning on the microstructure evolution and electrochemical properties of a martensitic stainless steel. *Corros Sci* 2016; 103: 95–104.

21. Tobata J, Ngo-Huynh KL, Nakada N, et al. Role of silicon in quenching and partitioning treatment of low-carbon martensitic stainless steel. *ISIJ Int* 2012; 52: 1377–1382.

22. Dai ZB, Chen H, Ding R, et al. Fundamentals and application of solid-state phase transformations for advanced high strength steels containing metastable retained austenite. *Mater Sci Eng: R* 2012; 143: 100590.

23. Kim B, Sietsma J and Santofimia MJ. The role of silicon in carbon partitioning processes in martensite/austenite microstructures. *Mater Des* 2017; 127: 336–345.

24. Bhadeshia H and Honeycombe R. *Steels: Microstructure and properties (Fourth edition)*. Kidlington: Butterworth-Heinemann, 2017.

25. Krauss G. Solidification, segregation, and banding in carbon and alloy steels. *Metall Mater Trans B* 2003; 34: 781–792.

26. HajyAkbary F, Sietsma J, Miyamoto G, et al. Interaction of carbon partitioning, carbide precipitation and bainite formation during the Q&P process in a low C steel. *Acta Mater* 2016; 104: 72–83.

27. HajyAkbary F, Sietsma J, Petrov RH, et al. A quantitative investigation of the effect of Mn segregation on microstructural properties of quenching and partitioning steels. *Scr Mater* 2017; 137: 27–30.

28. Arlazarov A, Gouné M, Bouaziz O, et al. Evolution of microstructure and mechanical properties of medium Mn steels during double annealing. *Mater Sci Eng A* 2012; 542: 31–39.

29. Hidalgo J, Celada-Casero C and Santofimia MJ. Fracture mechanisms and microstructure in a medium Mn quenching and partitioning steel exhibiting macrosegregation. *Mater Sci Eng A* 2019; 754: 766–777.

30. Zhang RJ, Zheng CL, Lv B, et al. Effect of non-uniform microstructure on rolling contact fatigue performance of bainitic rail steel. *Int J Fatigue* 2022; 159: 106795.

31. Forouzan F, Borasi L, Vuorinen E, et al. Optimization of quenching temperature to minimise the micro segregation induced banding phenomena in quenching and partitioning (Q&P) steels. *Steel Res Int* 2019; 90: 1800281.

32. Meng LX, Lu HH, Li WQ, et al. High strength and plasticity of AISI 430 ferritic stainless steel achieved by a recrystallisation annealing before quenching and partitioning process. *Mater Sci Eng A* 2021; 814: 141191.

33. Luo G, Li HY, Li YG, et al. Microstructures and properties of a low-carbon-chromium ferritic stainless steel treated by a quenching and partitioning process. *Mater* 2019; 12: 1704.

34. Mola J and De Cooman BC. Quenching and partitioning (Q&P) processing of martensitic stainless steels. *Metall Mater Trans A* 2013; 44: 946–967.

35. Huang QL, Volkova O, Biermann H, et al. Dilatometry analysis of dissolution of Cr-rich carbides in martensitic stainless steels. *Metall Mater Trans A* 2017; 48: 5771–5777.

36. Yang JR, Yu TH and Wang CH. Martensitic transformations in AISI 440C stainless steel. *Mater Sci Eng A* 2006; 438–440: 276–280.

37. Seo EJ, Cho L and De Cooman BC. Application of quenching and partitioning processing to Medium Mn steel. *Metall Mater Trans A* 2015; 46: 27–31.

38. Armstrong JT. Quantitative elemental analysis of individual microparticles with electron beam instruments. In: Heinrich KFJ and Newbury DE (eds) *Electron probe quantitation*. Boston, MA: Springer US, 1991, pp. 261–315.

39. Hu S, Mao YZ, Liu XB, et al. Intergranular corrosion behavior of low-chromium ferritic stainless steel without cr-carbide precipitation after aging. *Corros Sci* 2020; 166: 108420.

40. Raami L and Peura P. Influence of initial quenching on the microstructure and mechanical properties of quenched and partitioned ferritic stainless steels. *Metall Mater Trans A* 2022; 847: 143339.

41. Lee SJ and Van Tyne CJ. A kinetics model for martensite transformation in plain carbon and low-alloyed steels. *Metall Mater Trans A* 2012; 43: 422–427.

42. Seo EJ, Cho L and De Cooman BC. Modified methodology for the quench temperature selection in quenching and partitioning (Q&P) processing of steels. *Metall Mater Trans A* 2016; 47: 3797–3802.

43. Van Bohemen SMC and Sietsma J. Martensite formation in partially and fully austenitic plain carbon steels. *Metall Mater Trans A* 2009; 40A: 1059–1068.

44. Celada-Casero C, Sietsma J and Santofimia MJ. The role of the austenite grain size in the martensitic transformation in low carbon steels. *Mater Des* 2019; 167: 107625.

45. Babu SR, Ivanov D and Porter D. Influence of microsegregation on the onset of the martensitic transformation. *ISIJ Inter* 2019; 59: 169–175.